Advances in Nano Research, *Vol. 13, No. 2 (2022) 199-206*
https://doi.org/10.12989/anr.2022.13.2.199

Taguchi method-optimized roll nanoimprinted polarizer integration in high-brightness display

Dae-Young Lee[1], Jung-Gun Nam[1], Kang-Soo Han[2], Yun-Jong Yeo[1],
Useung Lee[3], Sang-Hwan Cho*[1] and Jong G. Ok**[3]

[1] *Display Research Center, Samsung Display, 1 Samsung-ro, Yongin-si, Gyeonggi-do, 17113 Korea*
[2] *Large Display Process Development Team, Samsung Display, 1 Samsung-ro, Yongin-si, Gyeonggi-do, 17113 Korea*
[3] *Department of Mechanical and Automotive Engineering, Seoul National University of Science and Technology, 232 Gongneung-ro, Nowon-gu, Seoul 01811, Korea*

(*Received July 16, 2021, Revised July 21, 2022, Accepted July 26, 2022*)

Abstract. We present the high-brightness large-area 10.1” in-cell polarizer display panel integrated with a wire grid polarizer (WGP) and metal reflector, from the initial design to final system development in a commercially feasible level. We have modeled and developed the WGP architecture integrated with the metal reflector in a single in-cell layer, to achieve excellent polarization efficiency as well as brightness enhancement through the light recycling effect. After the optimization of key experimental parameters via Taguchi method, the roll nanoimprint lithography employing a flexible large-area tiled mold has been utilized to create the 90 nm-pitch polymer resist pattern with the 54.1 nm linewidth and 5.1 nm residual layer thickness. The 90 nm-pitch Al gratings with the 51.4 nm linewidth and 2150 Å height have been successfully fabricated after subsequent etch process, providing the in-cell WGPs with high optical performance in the entire visible light regime. Finally we have integrated the WGP in a commercial 10.1” display device and demonstrated its actual operation, exhibiting 1.24 times enhancement of brightness compared to a conventional film polarizer-based one, with the contrast ratio of 1,004:1. Polarization efficiency and transmittance of the developed WGPs in an in-cell polarizer panel achieve 99.995 % and 42.3 %, respectively.

Keywords: in-cell polarizer; large-area display; roll nanoimprint lithography; Taguchi method; tiling method; wire grid polarizer

1. Introduction

For the past few years, many researchers have attempted to develop wire grid polarizers (WGPs) in information displays and imaging devices because of their excellent theoretical polarization efficiency, brightness enhancement, and design freedom (Pate *et al*. 2006, Cho 2018, Simioniuc *et al*. 2018). The WGP structure centrally comprises of the sub-100 nm-sized parallel metallic gratings directly patterned on the substrate. WGPs can enhance the brightness of display by recycling the s-polarization light component, while conventional film polarizers absorb it (see Fig. 1). Since a WGP is fabricated directly onto the substrate through the thin-film process, it is substantially thinner and lighter than a conventional film polarizer. The major parameters of WGP structures, such as grating pitch, linewidth, and height of the grid elements, determine the performance (*i.e*., extinction ratio and transmittance, in particular) (Im *et al*. 2018, Qin *et al*. 2019, Wang *et al*. 2021). To achieve sufficient polarization efficiency (PE) in the visible light wavelength regime, ultra-fine pitch and high aspect-ratio structures are required (Wu *et al*. 2013, Yeon *et al*. 2013, Schlachter *et al*. 2016). Accordingly, the fabrication processes become more complex, especially when aiming for high optical performance and large area. Recently reported WGPs in the field of displays showed the performances no larger than 20,000:1 extinction ratio (which corresponds to 99.99% PE) or 40% transmittance because of the challenges to the fabrication of ultra-fine pitch gratings and structural defects caused by trimming or oblique deposition process (Wu *et al*. 2013, Yeon *et al*. 2013). Moreover, the active width of a WGP panel has been usually smaller than 100-200 mm because the size of the master molds used for nanoimprint lithography are mostly limited within the 8″ diameter.

Addressing these issues, we present a highly scalable and reproducible WGP fabrication by using the UV roll nanoimprint lithography (R-NIL) on glass substrates for a commercially-feasible 10.1”-sized tablet panel. While many techniques involving such as solution processing and chemical etching are available for WGP fabrication (Kang *et al*. 2018, Verrier *et al*. 2015, Yamada and Ishihara 2016, Yamada and Yoshida 2020), the NIL-based approach has shown incomparable advantages involving precise and high-aspect ratio pattern definition, great reproducibility, fast processing speed, and so on (Chen *et al*. 2007, Schlachter *et al*. 2016, Shin *et al*. 2012, 2013, Yamada *et al*. 2012). R-NIL can further extend the scalability and productivity of the NIL-based WGP fabrication by using a flexible roller mold (Ahn *et al*. 2007, Wu *et al*. 2013). In this work, we have developed the flexible R-NIL mold by

*Corresponding author, Corporate VP,
E-mail: sh0825.cho@samsung.com
**Co-corresponding author, Professor,
E-mail: jgok@seoultech.ac.kr

Copyright © 2022 Techno-Press, Ltd.

ISSN: 2287-237X (Print), 2287-2388 (Online)

replicating from the master mold formed on a Si wafer (300 mm in the diameter) with the 90 nm grating pitch without recognizable seams between reticles. By using NIL, the in-cell polarizer panels integrated with WGPs and metal reflectors have been demonstrated for the first time in the world. Additional brightness enhancement has been achieved through the light recycling effect in the non-aperture area between the backlight unit and glass substrate.

2. Theoretical model for bright enhancement in the display panel

Architecturing the in-cell WGP in conjunction with the metal reflector is the key feature of the high-brightness display panels developed in this study. The film polarizer and dual brightness enhancement film (DBEF) in the conventional panels (Fig. 1(a)) are replaced to the wire grid polarizer and the metal reflector in the in-cell polarizer panel. The Al reflector can enhance the brightness through recycling of light in the non-aperture area as schematically shown in Fig. 1(b).

The bright enhancement features for conventional film-based and WGP/reflector-based panels are comparatively analyzed through the detailed theoretical calculations. The governing equations for the brightness enhancement of the conventional panel are derived as follows:

$$T_{Total,Ref.} = T_r + \alpha R_r T_r + \alpha^2 {R_r}^2 T_r + \cdots = \frac{T_r}{(1-\alpha R_r)} \tag{1}$$

$$E_{Ref.} = \frac{T_{total,Ref.}}{T_r} = \frac{1}{(1-\alpha R_r)} \tag{2}$$

where $T_{Total,\ Ref.}$ is the intensity of the light passing through the conventional panel with a film polarizer, and $E_{Ref.}$ denotes the brightness enhancement which is estimated to be ~1.3 in the presence of a DBEF.

The model equations for the brightness enhancement of the in-cell polarizer panel, on the other hand, are derived as follows:

$$\begin{aligned} T_{Total,\frac{WGP}{MR}} &= AT_{WGP} + (\alpha AR_{WGP} + \alpha(1-A)R'_{MR})AT_{WGP} \\ &+ \left((\alpha AR_{WGP} + \alpha(1-A)R'_{MR})\alpha(1-A)R'_{MR}\right)AT_{WGP} \\ &+ \left((\alpha AR_{WGP} + \alpha(1-A)R'_{MR})\alpha AR_{WGP}\right)AT_{WGP} + \cdots \\ &= \frac{AT_{WGP}}{1-[\alpha AR_{WGP} + \alpha(1-A)R'_{MR}]} \end{aligned} \tag{3}$$

$$E_{\frac{WGP}{MR}} = \frac{T_{Total,\frac{WGP}{MR}}}{T_{WGP}} = \frac{A}{1-[\alpha AR_{WGP} + \alpha(1-A)R'_{MR}]} \tag{4}$$

where $T_{Total,\ WGP/MR}$ and A are the intensity of the light passing through the WGP and metal reflector and the aperture ratio, respectively. It is a function of the aperture ratio (A) unlike the case with film polarizer and DBEF. $E_{WGP/MR.}$ denotes the brightness enhancement by the metal reflector. Consequently, the brightness enhancement (BE_{ICP}) of the in-cell polarizer panel compared to that of the conventional panel is as follows;

$$BE_{ICP} = \frac{T_{Total,WGP/MR}}{AT_{Total,Ref.}} = \frac{T_{WGP}(1-\alpha R_r)}{[1-\{\alpha AR_{WGP} + \alpha(1-A)R'_{MR}\}]T_r} \tag{5}$$

Table 1 parameters for brightness enhancement model

Parameters	Symbol	Value
Transmittance of film polarizer	T_r	0.42
Reflectance of the film polarizer (DBEF)	R_r	†0.45
Recycling efficiency of back light unit	α	‡0.51
Transmittance of WGP	T_{WGP}	0.42
Reflectance of WGP	R_{WGP}	0.44
Reflectance of metal reflector	R'_{MR}	0.9

†Rr is calculated from the typical brightness enhancement with DBEF 1.3.
‡α is calculated by comparing the metal black matrix and organic black matrix on the glass with the backlight unit. The reflectance from the organic black matrix is supposedly near zero.

Fig. 1(c) shows the prediction of brightness enhancement based on the light recycling model enabled by the WGP and reflector, where the brightness enhancement is plotted as a function of the aperture ratio. The brightness enhancement of ~20% is estimated for the aperture ratio of 42.9% in this study. The related parameters used in the above analysis are listed in Table 1. The analysis indicates that the reflector-integrated WGP additionally enhances brightness above the DBEF-based performance, and the level of enhancement increases with decreasing aperture ratio. Therefore, it suggests that the reflector-integrated WGP architectures reversely utilize the relatively low aperture ratio which used to be the constraint in conventional operation of high-resolution panels.

3. Design and optimization of master mold and roll nanoimprint lithography

3.1 Design and fabrication of a nanoimprint master mold

A rigorous coupled-wave analysis (RCWA) model (G-Solver, ver. 5.2) was adopted to determine the WGP period that can meet the satisfactory extinction ratio (*i.e.*, larger than 20,000) and balanced transmission throughout the entire visible light wavelength. Figs. 2(a) and (b) show the extinction ratio and transmission plots for three visible light wavelengths representing red (750 nm), green (550 nm), and blue (380 nm), for the 1500 Å-high, 1:1 duty (*i.e.*, ratio of linewidth to spacing) gratings with varied WGP pitches. As shown in Fig. 2(a), the WGP pitch should be below 100 nm to achieve the extinction ratio of 20,000 when the Al grating height is 1500 Å. Fig. 2(b) reveals that the WGP pitch needs to be ~100 nm to balance the color transmissions of red, green, and blue with less than 10 % discrepancy. For

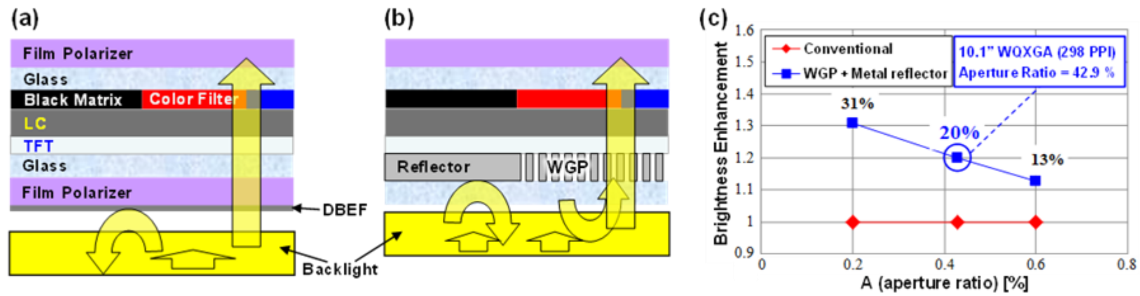

Fig. 1 Schematic structures of liquid crystal displays (LCD) with (a) conventional absorptive film polarizer and (b) WGP embedded with a metal reflector; (c) Prediction of brightness enhancement as a function of the aperture ratio for conventional and Al reflector-integrated WGP panels

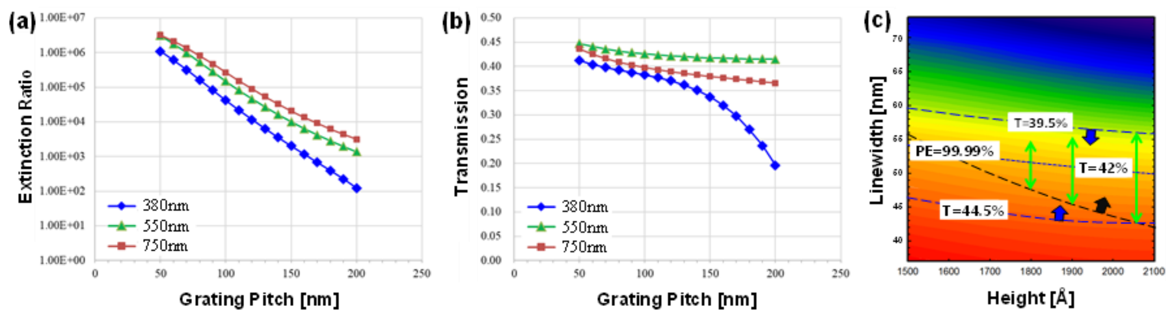

Fig. 2 Extinction ratio (a) and transmission (b) of the 1500 Å-high, 1:1 duty gratings with different pitches for three wavelengths of 380, 550, and 750 nm; (c) Contour plot of polarization efficiency (PE) and transmission (T) depending on the linewidth and height of a 90 nm-pitch WGP

reliable semiconductor photolithography, we have decided the final WGP pitch to be 90 nm.

PE and optical transmittance are two most important factors determining the WGP performance in the display panel. For applying to a commercial display, we aim that the WGP can achieve 99.99 % or higher PE and 42 % or higher transmittance. Notably, the higher the grating, generally the better the PE (Verrier *et al.* 2015). However, the fabrication difficulty generally increases for higher aspect-ratio gratings. Hence, an optimal grating height should be defined by considering both perspectives. Fig. 2(c) shows the contour simulation result of transmission as well as PE of the 90 nm-pitch WGP; it suggests that the performance greater than 99.99 % PE and 42 % transmittance be expected for the Al grating with the height between 1700 Å and 2100 Å. Here, the acceptable linewidth range extends as the grating height increases; for instance, the linewidths of the 1700 Å- and 2100 Å-high gratings should be 50-52.5 nm (~2.5 nm margin) and 42.5-50 nm (~7.5 nm margin), respectively, to satisfy PE > 99.99 % and transmittance > 42 %. The larger margin for linewidth variation can lead to more reasonable and reliable fabrication. This let us consider the aspect ratio of WGP grating may be 4 or higher during the fabrication, as will be actually demonstrated later in this paper.

Fabrication of the above designed structure as the flexible R-NIL master mold is one of the most elaborated parts in this study. An immersion lithography (Immersion Scanner 1950i, ASML, Netherland) was applied to fabricate the original master on a Si wafer (300 mm in the diameter). The minimum feature size achievable in this lithography is 36 nm at 193 nm exposure wavelength and 1.35 numerical aperture (NA). Figs. 3(a) and (b) show the optical and scanning electron microscopy (SEM) images of the fabricated 300 mm-diameter Si master mold. The in-depth critical dimension (CD) analysis imaging discloses that the nanograting dimensions are 108.31 nm in the height and 45.05 nm and 52.8 nm in the half and bottom linewidths, respectively (Figs. 3(c) and (d)).

By performing the ‘tiling’ process using this Si master on a flexible polyethylene terephthalate (PET) film, we could fabricate the large-area flexible mold for the subsequent R-NIL process (Figs. 3(e) and (f)). In the tiling process, the Si master was first replicated onto a PET film through the UV imprinting using a UV-curable, optically-transparent resin such as polyurethane acrylate (PUA). The PET replica was then repeatedly stamped in a slightly overlapped fashion on the large-area PET film coated with PUA. A careful control of resin dispensing and mold contacting and rolling conditions enables the seam minimization, as demonstrated in Fig. 3(g). Further details of essential principle and experimental control of the tiling process can be found elsewhere (Kwak *et al.* 2015). Briefly here, once the first-round stamping and resin curing were done, the second-round stamping were performed side by side, each following the sequence of the PUA resin dispensing, PET mold contacting and rolling, UV curing, and demolding; this job could be repeated until the total tiled area reaches at the desired level, for instance, large enough to cover the 10.1” display panel area.

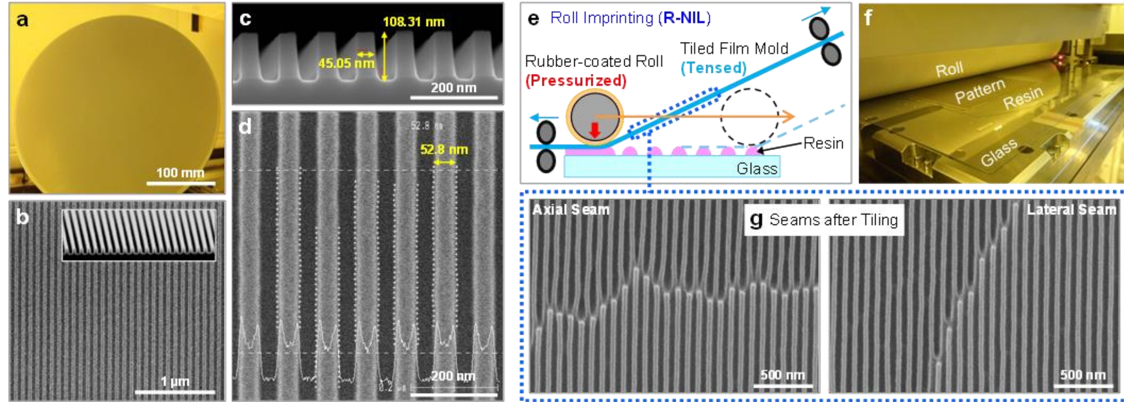

Fig. 3 Optical image (a) and SEM image (b) of a 300 mm-diameter Si master mold for NIL; An inset to (b) shows the perspective SEM view; Enlarged SEM images of (c) cross-sectional view and (d) top view for CD analysis; Scheme (e) and actual system (f) of the R-NIL process, where the large-area flexible mold fabricated by the tiling process with minimal seams (g) is employed

Table 2 Parameters and levels for design of experiments

Parameters	Unit	Level 1	Level 2	Level 3
Roll Pressure	[kPa]	100	300	500
Roll Speed	[mm/s]	0.5	1.0	5.0
Dispensing Volume	[μl]	10	15	30

Table 3 Sample configuration in the l9 orthogonal array experiment using taguchi method

Experiment No.	* Variable (parameters)		
	Roll Pressure	Rolling Speed	Dispensing Volume
1	100	0.5	10
2	100	1.0	15
3	100	5.0	30
4	300	0.5	15
5	300	1.0	30
6	300	5.0	10
7	500	0.5	30
8	500	1.0	10
9	500	5.0	15

3.2 Optimization of the roll nanoimprint lithography by Taguchi method

We can the estimate residual layer thickness (RLT; h_f [m]) in the R-NIL process, based on the polymer flow's squeeze model (Ahn and Guo 2009, Reddy and Bonnecaze 2005, Rowland *et al*. 2005) given as Eq. (6):

$$h_f = \left(\frac{2F}{\mu a^2 LV} + \frac{1}{h_0^2}\right)^{-1/2} \tag{6}$$

where μ [cP], a [m], L [m], and F [N] represent viscosity and contact length for the direction perpendicular to the rolling direction, contact length for the rolling direction, and applying force from a roll, respectively. h_o [m] and V [m/s] denote initial thickness and roll velocity in the rolling direction. This equation indicates that main parameters of a R-NIL process are initial coating thickness, pressure, and roll velocity. Therefore, in this study, variables and levels for experimental design are used in the RLT optimization as shown in Table 2. The RLT has been an important factor in NIL because it can affect the profile and uniformity of critical dimension of linewidth after post dry etching process. Of note, we used a NIP-K28 resin (Chemoptics, Korea, μ=8 cP, surface tension=47 mN/m) for our R-NIL process.

Now the NIL process parameter values can be optimized in order to improve the process quality. Among various experimental design methods, the Taguchi method utilizes a special design of orthogonal arrays that allows to study the whole parameter space with a reduced number of experiments (Taguchi 1990), which has been effective in many diverse studies (Gulcan and Karahan 2021, Zhang *et al*. 2021, Nezadi *et al*. 2021, Prusty *et al*. 2015). Table 3 shows sample configuration in the L9 orthogonal array using Taguchi experimental design for the RLT optimization.

Fig. 4 represents the influences of the roll pressure, rolling speed, and dispensing volume, explained in terms of S/N (signal-to-noise ratio) (Fig. 4(a)) and average RLT value (Fig. 4(b)) calculated through the Taguchi method. Here the RLT could be optimized such that it would be uniform and minimal. In the Taguchi method, the S/N ratio is a logarithmic function used to optimize fabrication process or product design, minimizing the variability. The formula for the smaller-is-better S/N ratio using base 10 log is:

$$\frac{S}{N} = -10log\left(\frac{1}{n}\sum_{i=1}^{n} y_i^2\right) \tag{7}$$

where n is the number of responses in the factor level combination. y_i denotes the results of the *i*-th performance characteristic value. The S/N ratio can be also understood as the inverse of variance. Namely, the maximization of S/N ratio allows reduction of the variability of the process against undesirable changes in neighboring environment (also named uncontrollable factors or factors of noise). To minimize variability, the level of factor which produces the greatest value of S/N ratio must be chosen.

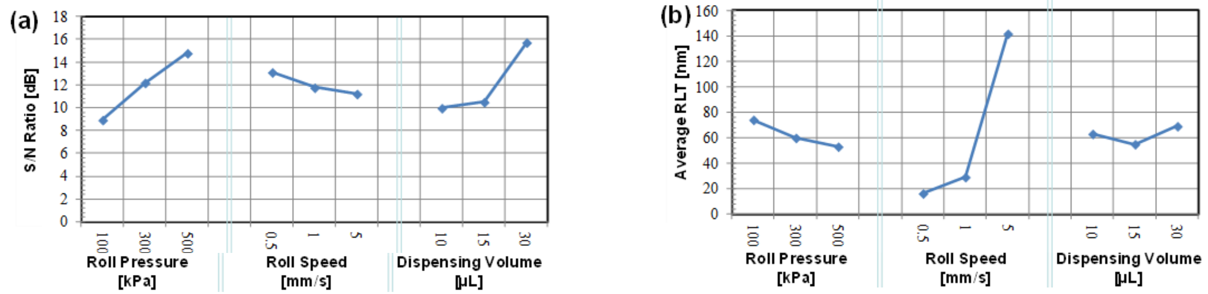

Fig. 4 (a) S/N ratio and (b) average value of the RLTs calculated through the Taguchi method

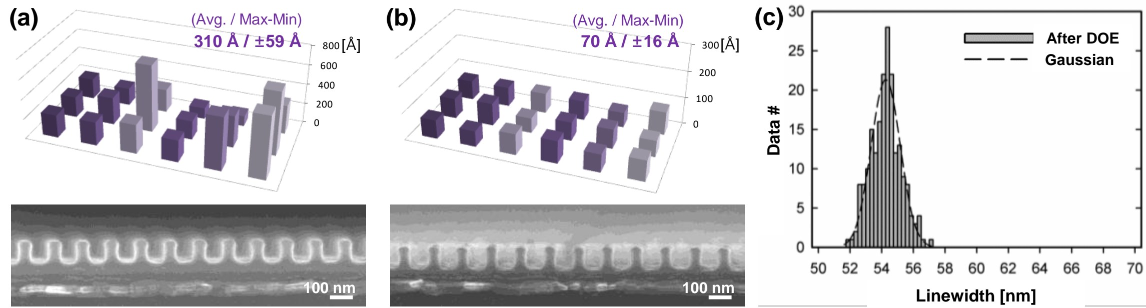

Fig. 5 RLT distribution in NIL (a) before and (b) after applying the Taguchi method (unit = [Å]); The SEM images for each case are shown in the bottom; (c) Gaussian distribution of linewidths after applying the Taguchi method-based design of experiment (optimized condition)

Accordingly, the levels of parameters of roll pressure, roll speed, and dispensing volume are chosen to be 500 kPa, 0.5 mm/s, and 30 μl, respectively. Notably, roll speed is not a main parameter in the S/N ratio but a critical factor in the average value. It suggests that the roll speed can be used as control parameter which can control mean value without variability of data distribution. Figs. 5(a)-(b) show the RLT distributions in NIL before and after applying Taguchi method, respectively. Here RLT measurements were conducted for multiple points (up to 18) evenly picked up from the entire NIL-ed area. The RLTs are calculated to be 310±59 Å and 70±16 Å in the cases before and after applying optimization of factors, respectively. The optimal linewidth is given as 54.1 nm in average and the standard deviation is 0.95 nm in the optimization condition as shown in Fig. 5(c).

4. Development and characterization of the large-area high-brightness display panel

By using the above optimized design and implementation of the R-NIL process, the display panel with the in-cell 90 nm-pitch WGP embedded with a metal reflector is developed. The fabrication procedure is schematically shown in Fig. 6. The front surface was vacuum-deposited with 200 nm-thick Al and 15 nm-thick Ti. A 20 nm-thick silicon oxide (SiO_2) was then coated by chemical vapor deposition onto the Ti layer, which functions as a hard mask for subsequent metal (Al and Ti) etching steps. The UV R-NIL process was performed (EVG®7200 LA, EV Group; Fig. 3(f)) to form the 90 nm-pitch resist grating patterns with the thickness of ~100 nm. As previously investigated through the Taguchi method, the R-NIL process was optimized in terms of the dispensing volume, rolling speed, and roll pressure, to ensure a uniform and thin residual layer, as thin as 5.1 nm in average. This residual layer of a UV resist was then removed by the CF_4 plasma etching to expose the SiO_2 layer between the resist grating lines. After etching of the oxide by using a C_4F_8 plasma, a photolithography was performed to cover the non-aperture area, which eventually is left behind as the reflector. Lastly, using the SiOx pattern as a hard mask, a chlorine-based dry etch process was performed to etch all through the metal layers (Al and Ti) to form the Al-based WGP and reflector. Additional oxide etch process, named the breakthrough (BT) step, could be applied to remove the SiO_2 layer off the metal layers.

Fig. 7 demonstrates the fabrication results. Fig. 7(c) shows the 90 nm-pitch Al WGPs having the 51.4 nm linewidth and 2150 Å height (~4.2 aspect ratio) in the aperture area in a panel. Figs. 7(a)-7(b) show the SEM images of metal reflectors next to Al WGPs in the same panel pixel. Fig. 8(a) exemplifies the actual display operation (10.1”, WQXGA (Wide Quad Extended Graphics Array; 2560 × 1600 resolution) employing the in-cell polarizer panel incorporating WGPs and metal reflectors, implemented to a commercial product for the first time in the world. Figs. 8(b)-8(c) show the transmittance and PE of the fabricated WGPs before and after the BT step. We can verify that the BT step affects the WGP linewidth which controls the transmittance and PE. This characterization result also indicates that the variation of the WGP linewidth is reduced when the BT step is skipped. More importantly, it could be confirmed that the BT-applied WGPs with the linewidths of 50-54 nm in average and the Al height of

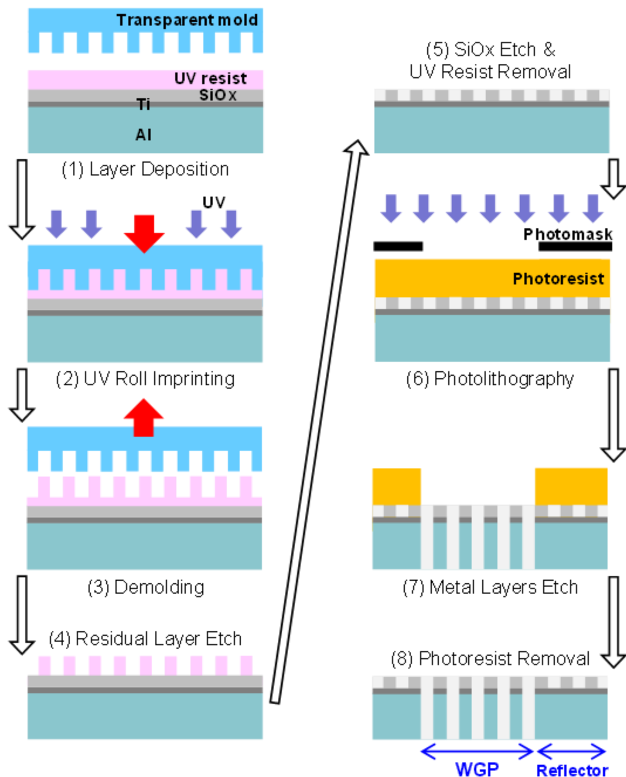

Fig. 6 Schematic diagram of the fabrication process of the in-cell WGP embedded with a metal reflector

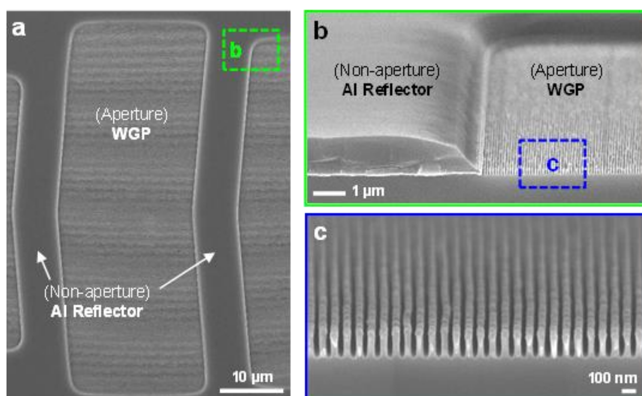

Fig. 7 SEM images of the fabricated in-cell WGP structures integrated with reflectors: (a) overview in a panel pixel, (b) WGP-reflector border area, and (c) enlarged view showing the WGP nanostructure

~2150 Å lead to the performances of PE greater than 99.99% transmittance higher than ~42%.

Namely, the PE, contrast ratio, and transmittance could finally achieve 99.995% (40,000:1 extinction ratio), 1,004:1, and 42.3%, respectively, in the actual display panel operation. The latter corresponds to 1.24 times enhancement of brightness at 522 nit. As a comparison, the average performance of the conventional panel employing the absorptive film polarizer and DBEF was 422 nit and contrast ratio of 925:1. The enhanced brightness and performance by integrating the WGP and reflector in the panel corroborates the prediction presented in Fig. 1(c). The

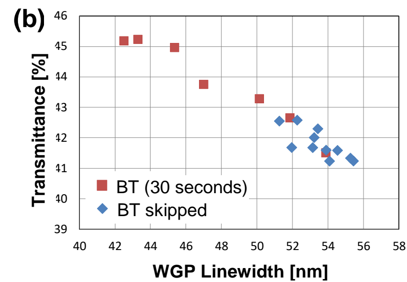

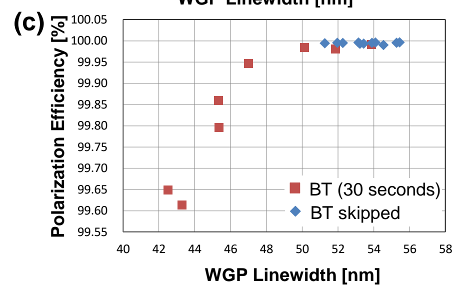

Fig. 8 (a) Operation image of the developed in-cell polarizer panel in a commercial 10.1″ PLS mode display device (WQXGA; 2560 × 1600 resolution). The upper-right white reflection is from the ambient lighting; Transmittance (b) and polarization efficiency (c) of the WGPs with and without a breakthrough (BT) step application

current study may thus be practically applied to the industrial manufacturing of high-brightness large-area displays, which is indeed on the way.

5. Conclusions

In summary, we have developed the large-area in-cell polarizer panel integrating the NIL-ed WGPs and metal reflectors for the first time in a commercially-feasible level, which achieves the brightness enhancement of 1.24 at 522 nit and the contrast ratio of 1,004:1. The Taguchi method-optimized R-NIL process enables the scalable and uniform fabrication of 90 nm-pitch Al gratings of the ~4.2 aspect ratio with the residual layer controlled to be as thin as 5.1 nm. The subsequent photolithography along with etching processes can create the reflector-integrated WGP structure in the same panel pixel. We have demonstrated that the in-cell polarizer panel with a metal reflector can enhance the brightness by recycling the light reflection, compared to the DBEF-incorporated conventional film polarizer-based panel, where the levels of enhancement increases with decreasing aperture ratio. Therefore, the architecture developed in this

work can address the critical issues in the high-resolution display that requires the brightness compensation as lowering the aperture ratios.

Acknowledgments

This work was supported by the National Research Foundation of Korea (NRF) grants funded by the Korean Government (No. 2022R1I1A2073224 and No. 2022M3 C1A3090850 (Ministry of Science and ICT (MSIT)). We thank Dr. Kinam Kim, Chairman of Samsung Electronics and the process development team of the Semiconductor R&D Center for their help in manufacturing of the master mold wafer.

References

Ahn, S.H. and Guo, L.J. (2009), "Large-area roll-to-roll and roll-to-plate nanoimprint lithography: A step toward high-throughput application of continuous nanoimprinting", *ACS Nano*, **3**(8), 2304-2310. https://doi.org/10.1021/nn9003633.

Ahn, S.H., Kim, J.S. and Guo, L.J. (2007), "Bilayer metal wire-grid polarizer fabricated by roll-to-roll nanoimprint lithography on flexible plastic substrate", *J. Vac. Sci. Technol. B*, **25**(6), 2388-2391. https://doi.org/10.1116/1.2798747.

Chen, L., Wang, J.J., Walters, F., Deng, X.G., Buonanno, M., Tai, S. and Liu, X.M. (2007), "Large flexible nanowire grid visible polarizer made by nanoimprint lithography", *Appl. Phys. Lett.*, **90**(6). https://doi.org/10.1063/1.2472532.

Cho, Y.T. (2018), "Fabrication of wire grid polarizer for spectroscopy application: From ultraviolet to terahertz", *Appl. Spectrosc. Rev.*, **53**(2-4), 224-245. https://doi.org/10.1080/05704928.2017.1328427.

Gulcan, M.F. and Karahan, B.D. (2021), "Designing carbon-supported Fe2O3 anodes for lithium ion batteries", *J. Appl. Electrochem.*, **51**(6), 917-931. https://doi.org/10.1007/s10800-021-01552-2.

Im, S., Sim, E. and Kim, D. (2018), "Microscale heat transfer and thermal extinction of a wire-grid polarizer", *Sci Rep*, **8**(1), 1-11. https://doi.org/10.1038/s41598-018-33347-5.

Kang, J., Yun, H.S., Jang, H.I., Kim, J., Park, J.H. and Lee, J.Y. (2018), "Solution-processed aluminum nanogratings for wire grid polarizers", *Adv. Opt. Mater.*, **6**(14). https://doi.org/10.1002/adom.201800205.

Kwak, M.K., Ok, J.G., Lee, S.H. and Guo, L.J. (2015), "Visually tolerable tiling (VTT) for making a large-area flexible patterned surface", *Mater. Horizons*, **2**(1), 86-90. https://doi.org/10.1039/C4MH00159A.

Nezadi, M., Keshvari, H. and Yousefzadeh, M. (2021), "Using Taguchi design of experiments for the optimization of electrospun thermoplastic polyurethane scaffolds", *Adv. Nano Res.*, **10**(1), 59-69. https://doi.org/10.12989/anr.2021.10.1.059.

Pate, M., Meyer, J., Shiefman, J. and Hansen, D. (2006), "Wire-grid polarizers in modern LCOS light-engine configurations", *J. Soc. Inf. Disp.*, **14**(3), 275-283. https://doi.org/10.1889/1.2185276.

Prusty, R., Mukharjee, B.B. and Barai, S.V. (2015), "Nano-engineered concrete using recycled aggregates and nano-silica: Taguchi approach", *Adv. Concr. Constr.*, **3**(4), 253-268. http://doi.org/10.12989/acc.2015.3.4.253.

Qin, L., Yang, J.T., Wang, C.G., Shen, C., Wang, Y.B., Tang, J. and Liu, J. (2019), "Preparation and measurement of subwavelength bilayer metal wire grid polarizers on flexible plastic substrates", *Opt. Commun.*, **434**, 118-123. https://doi.org/10.1016/j.optcom.2018.10.060.

Reddy, S. and Bonnecaze, R.T. (2005), "Simulation of fluid flow in the step and flash imprint lithography process", *Microelectron. Eng.*, **82**(1), 60-70. https://doi.org/10.1016/j.mee.2005.06.002.

Rowland, H.D., Sun, A.C., Schunk, P.R. and King, W.P. (2005), "Impact of polymer film thickness and cavity size on polymer flow during embossing: toward process design rules for nanoimprint lithography", *J. Micromech. Microeng.*, **15**(12), 2414-2425. https://doi.org/10.1088/0960-1317/15/12/025.

Schlachter, F., Barnett, J., Plachetka, U., Nowak, C., Messerschmidt, M., Thesen, M. and Kurz, H. (2016), "UV-NIL based nanostructuring of aluminum using a novel organic imprint resist demonstrated for 100 nm half-pitch wire grid polarizer", *Microelectron. Eng.*, **155**, 118-121. https://doi.org/10.1016/j.mee.2016.03.046.

Shin, Y.J., Pina-Hernandez, C., Wu, Y.K., Ok, J.G. and Guo, L.J. (2012), "Facile route of flexible wire grid polarizer fabrication by angled-evaporations of aluminum on two sidewalls of an imprinted nanograting", *Nanotechnology*, **23**(34), 6. https://doi.org/10.1088/0957-4484/23/34/344018.

Shin, Y.J., Wu, Y.K., Lee, K.T., Ok, J.G. and Guo, L.J. (2013), "Fabrication and encapsulation of a short-period wire grid polarizer with improved viewing angle by the angled-evaporation method", *Adv. Opt. Mater.*, **1**(11), 863-868. https://doi.org/10.1002/adom.201300276.

Simioniuc, C.C., Rizea, A. and Marin, C. (2018), "Review of polarization components for infrared imaging systems: from wire-grid structured surfaces to reconfigurable metasurfaces", *J. Optoelectron. Adv. Mater.*, **20**(5-6), 236-246.

Taguchi, G. (1990), *Introduction to Quality Engineering*, McGraw-Hill, New York, U.S.A.

Verrier, I., Kampfe, T., Celle, F., Cazier, A., Guttmann, M., Matthis, B., Laukkanen, J., Lacour, F., Veillas, C., Reynaud, S., Parriaux, O. and Jourlin, Y. (2015), "Wire-grid polarizer using galvanic growth technology: demonstration of a wide spectral and angular bandwidth component with high extinction ratio", *Opt. Eng.*, **54**(4). https://doi.org/10.1117/1.OE.54.4.047105.

Wang, C.H., Lai, D.S., Fan, Y., Tian, H.M., Li, X.M., Chen, X.L. and Shao, J.Y. (2021), "Nanoimprinting metal-containing nanoparticle-doped gratings to enhance the polarization of light-emitting chips by induced scattering", *Nanotechnology*, **32**(23). https://doi.org/10.1088/1361-6528/abe964.

Wu, C.L., Sung, C.K., Yao, P.H. and Chen, C.H. (2013),

"Sub-15 nm linewidth gratings using roll-to-roll nano-imprinting and plasma trimming to fabricate flexible wire-grid polarizers with low colour shift", *Nanotechnology*, **24**(26). https://doi.org/10.1088/0957-4484/24/26/265301.

Yamada, I. and Ishihara, Y. (2016), "Fabrication of infrared wire-grid polarizer by sol-gel method and soft imprint lithography", *Appl. Phys. Express*, **9**(5). https://doi.org/10.7567/APEX.9.052202.

Yamada, I., Yamashita, N., Tani, K., Einishi, T., Saito, M., Fukumi, K. and Nishii, J. (2012), "Infrared wire-grid polarizer with antireflection structure by imprinting on both sides", *Appl. Phys. Express*, **5**(8). https://doi.org/10.1143/APEX.5.082502.

Yamada, I. and Yoshida, R. (2020), "Fabrication of an infrared wire-grid polarizer via anisotropical Si etching in KOH solution", *Appl. Optics*, **59**(18), 5570-5575. https://doi.org/10.1364/AO.392883.

Yeon, J., Lee, Y.J., Yoo, D.E., Yoo, K.J., Kim, J.S., Lee, J., Lee, J.O., Choi, S.J., Yoon, G.W., Lee, D.W., Lee, G.S., Hwang, H.C. and Yoon, J.B. (2013), "High throughput ultralong (20 cm) nanowire fabrication using a wafer-scale nanograting template", *Nano Lett*., **13**(9), 3978-3984. https://doi.org/10.1021/nl400209n.

Zhang, F.B., Wang, M. and Yang, M.Y. (2021), "Successful application of the Taguchi method to simulated soil erosion experiments at the slope scale under various conditions", *Catena*, **196**, 104835. https://doi.org/10.1016/j.catena.2020.104835.

JL